SPE-191462-18IHFT-MS

Analytical Model for Predicting Fracture Initiation Pressure from a Cased and Perforated Wellbore

X. Weng, L. Xu, O. Magbagbeola, K. MacPhail, and N. Uschner, Schlumberger; B. J. Carney, Northeast Natural Energy LLC

This paper was prepared for presentation at the SPE International Hydraulic Fracturing Technology Conference and Exhibition held in Muscat, Oman, 16 - 18 October 2018.

Abstract

Although clustered perforations have become a primary choice of completion for horizontal wells in the development of low-permeability reservoirs, downhole measurements and production logging often indicate nonuniform production from the perforation clusters, with some of them not stimulated or not contributing to the production. One of the mechanisms contributing to this is nonuniform/inefficient breakdown of the perforations. However, being able to assess the effectiveness of perforation breakdown because of lateral variation of the formation properties and stresses is challenging, not only because of the lack of the data, but also because of the lack of a practical engineering model to predict the fracture initiation and breakdown pressures for cased and perforated completions due to the complexity of well configuration and perforation geometry. In this paper, an analytical fracture initiation model is presented along with the comparison against 3D numerical simulations and published experimental data. The breakdown pressure data from a Marcellus shale horizontal test well in the US Department of Energy (DOE)–sponsored Marcellus Shale Energy and Environmental Laboratory consortium are analyzed and compared to the model prediction using the high-resolution 1D mechanical earth model derived from high-tier logs.

Introduction

While the clustered perforations have become a primary choice of completion for horizontal wells in the development of low-permeability reservoirs, downhole measurements often indicate nonuniform fluid distribution during stimulation treatment (Molenaar et al. 2013; Ugueto et al. 2016). Similarly, post-stimulation production logging also indicates some of the perforation clusters not contributing to the production at all (Miller et al. 2011). There are multiple possible causes for this behavior, among which are uneven flow distribution among perforation clusters due to insufficient limited-entry perforation friction to overcome the stress difference to distribute the flow evenly among the clusters; proppant erosion of the perforations, especially for the heel clusters, that negates the limited-entry effect (Somanchi et al. 2016); and possibly the stress shadow interference among the propagating fractures. To mitigate the negative effect of heterogeneous rock properties and stresses among different perforation clusters in the same pumping

stage, a customized completion strategy that places perforation clusters at depths with similar properties has been employed when lateral measurements are available. The lateral is usually grouped into sections based on petrophysical and geomechanical properties that define reservoir quality and completion quality. The engineered completion generally had a positive impact on achieving more uniform flow distribution and well productivity (Cipolla et al. 2011; Slocombe et al. 2013; Walker et al. 2012; Wutherich et al. 2012).

However, one factor that may not have received sufficient attention is the fracture initiation process from the perforations. Wellbore and formation conditions can be such that some of the perforation clusters may not be broken down at all, and hence unstimulated, or breakdown may be limited to only a few perforations within a cluster that have initiated or connected to the fracture, restricting the flow into the fracture. Understanding how perforation completion and formation parameters affecting the fracture initiation process will help in identifying potential fracture initiation and breakdown issues in a given formation and adjusting perforation cluster design accordingly to achieve more uniform fracture initiation and flow distribution across all perforation clusters.

It is well known that perforation density, phasing, and orientation impact the geometry and initiation pressure of the hydraulic fracture(s) from a perforated vertical wellbore (Behrmann and Elbel 1991; Behrmann and Nolte 1998). El Rabaa (1989) and Abbas et al. (1996) conducted extensive laboratory block experiments to study fracture initiation from perforated boreholes and suggested short perforation interval as a preferred strategy to minimize propagating multiple competing fractures from the same perforation interval that can cause fracture width restrictions, which had become a general practice for cased horizontal well plug-and-perf completions. An extensive experimental program and theoretical work were conducted by Weijers and de Pater (1992, 1994), Weijers et al. (1994), and van de Ketterij and de Pater (1997) to study fracture initiation from horizontal and deviated, both open and cased-perforated, wellbores. Work by van de Ketterij and de Pater showed that for high-angle deviated or horizontal wells, multiple starter fractures originating from the spirally phased perforations may not connect to form a single fracture plane, but rather stay as separate, horizontally offset transverse fractures circumferentially spread out around the borehole to form a fan-like structure. This is schematically illustrated in Fig. 1.

Significantly improved understanding was obtained from the observations in the extensive laboratory experiments over the years, which provided valuable insights and guidance in well completion practices. These experiments revealed a very complex near-wellbore fracture initiation process and geometries, depending on many factors such as wellbore and perforation orientations; perforation size, depth, and spacing; in-situ stresses; rock properties; cement integrity; and fluid penetration into the cement annulus. Due to these complexities, and the strong coupling of rock mechanical deformation, failure, and stress field to fluid flow into the permeable rock and the initiated fractures, theoretical analyses and modeling of the fracture initiation process are very challenging and are limited in the literature. Fracture initiation or breakdown pressure is often estimated based on the classic elastic solution for an open borehole, using either the Hubert and Willis (1957) equation when the borehole is parallel to one of the in-situ principal stresses or, more generally, Kirsch's elastic solution for borehole not aligned with principal stresses (Yew and Li 1988; Thiercelin and Roegiers 2000), ignoring the effects of casing and perforations. Although it is possible that the fracture could initiate in the annulus rather than from perforations if the cement bonding is poor so that fluid easily penetrates and directly pressurizes on the rock face and if the perforations are significantly misaligned with the expected fracture plane, fractures commonly initiate from the base or tip of the perforation tunnels (Behrmann and Elbel, 1991). Yew et al. (1989) proposed to estimate the initiation pressure for perforations by treating the perforation as an isolated open hole, neglecting the influence of the wellbore. Hossain et al. (2000) used an analytical approach for estimating the initiation pressure from perforations by first computing the local stresses in the rock around the borehole wall based on the Kirsch solution, and then applying them as the remote stresses on the perforation, which is treated as a cylindrical open hole. This approximation is reasonable because the size of the perforation tunnel is much smaller than the size of the borehole. In their analysis, the casing was not considered, and it was assumed that the

wellbore fluid pressure is directly applied to the borehole wall and fracture initiation occurs at the base of the perforation. Besides analytical models, detailed numerical modeling of stress distribution around perforation tunnels and the initiation pressure has also been carried out using the finite element method (Yuan et al., 1995) and boundary element method (Alekseenko et al. 2012). Again, these studies mainly considered an uncased borehole. Limited simulations were also done for a cased hole by Yuan et al. (1995), but the far-field stress is applied as if on a precemented casing, whereas, in reality, casing is cemented with rock prestressed. The effect of pore pressure was not considered in these studies.

Recently, Waters and Weng (2016) presented an analytical model for predicting fracture initiation pressure for individual perforations, the breakdown pressure (peak pressure during a pumping operation), as well as the number of perforations broken down in a multiclustered cased and perforated completion. The model is based on the analytical elastic solution and an approach similar to that of Hossain et al. (2000), but includes the effect of casing, the prestress of the rock before cementing of the casing, and possible initiation from both the base and the tip of perforation tunnels. A series of sensitivity analyses were carried out to quantify the impact of injection rate, tectonic setting, stress variation between clusters, and perforation properties on hydraulic fracture creation, orientation, and complexity. It demonstrated that fractures may not initiate at many clusters and that within an active cluster some perforations may not be accepting fluid.

In this paper, we consider the effect of plastic yield around the perforation tunnel on initiation pressure and model validation against published numerical simulations and experimental data. The breakdown pressure data from a Marcellus horizontal test well in the US Department of Energy (DOE)–sponsored Marcellus Shale Energy and Environmental Laboratory (MSEEL) consortium are also analyzed and compared to the model prediction using the high-resolution 1D mechanical earth model derived from high-tier logs.

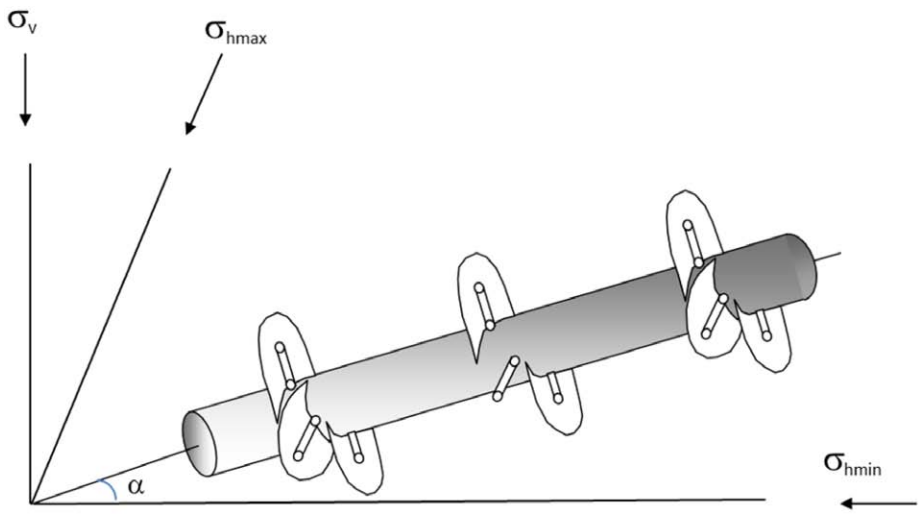

Figure 1—Diagram of multiple clusters of spiral perforations in a horizontal well and initial cracks originated from the perforations.

Model Description

When fracturing fluid is pumped into a cased wellbore at a high pump rate, the pressure rises rapidly until it exceeds the fracture initiation pressure to propagate fractures from at least some of the perforations. Fracture initiation pressure will vary for different perforations oriented at different angles and located at different depths (for a generally heterogeneous formation). The perforation with the lowest initiation pressure will break down first. However, the entire flow rate cannot be forced through one or a limited number of perforations due to very high perforation friction caused by a large flow rate per perforation. Consequently, the wellbore pressure will continue to rise with time, with the pumped fluid stored in the wellbore due to the limited flow rate that can be accommodated by the broken perforations. This subsequently leads

to more fractures being initiated from additional perforations with higher initiation pressure. This process continues until all the broken perforations can take the full pump rate at a wellbore pressure below the next initiation pressure among the remaining perforations. A peak pressure is hence reached, which is defined as the breakdown pressure of the treatment interval and can be observed in the treating pressure data.

To be able to predict the breakdown process, fracture initiation pressure from an arbitrarily oriented perforation needs to be estimated. To simplify the problem, certain assumptions are made in the model, including the following:

- The rock is assumed elastic and isotropic.
- The effect of fluid viscosity and pressurization rate on fracture initiation pressure is ignored.
- Potential delamination of the cement bond and subsequent fluid penetration into the cement micro-annulus and the associated pressure loss are not considered. Therefore, potential fracture initiation from a location in the cement annulus that is not coinciding with a perforation is not considered.
- The rock is assumed to have very low permeability, and the poroelastic effect is neglected.
- Stress perturbation due to the presence of the neighboring perforations is neglected, as is the interaction between the initiated fracture with the neighboring perforations.
- Additional pressure loss due to near-wellbore tortuosity is neglected.
- Potential mechanical damage of the rock or "stress cage" resulting from the perforating process is not considered.

For the estimate of fracture initiation pressure from a perforation, the perforation is considered as an idealized cylindrical open hole. The initiation pressure is determined using the elastic solution for an infinite open hole. Two most likely initiation sites will be considered: one at the base of the perforation and the other near the tip of the perforation. At each initiation site, the local stresses in the rock, taking into account the wellbore, will first be computed and then used as the "far-field stresses" applied on the perforation hole, as proposed by Hossain et al. (2000).

Fig. 2 illustrates the cross-section of a cased wellbore with a single perforation with perforation tunnel length of l_p. The wellbore consists of a cemented casing assumed to be concentric with the inside and outside radii of R_i and R_o, respectively; the borehole radius is r_w.

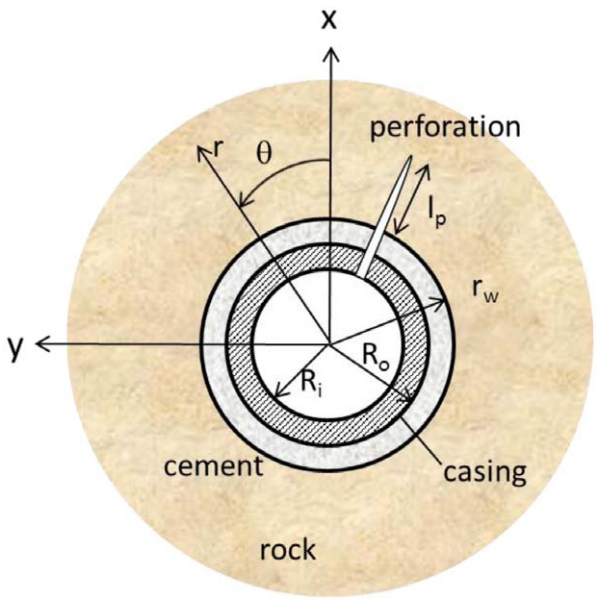

Figure 2—Diagram of wellbore cross section.

Based on the elasticity solution by Kirsch, the stress distribution is given below in the polar coordinates (r, θ) (Yew and Li 1988; Thiercelin and Roegiers 2000):

$$
\begin{aligned}
\sigma_r &= \frac{1}{2}\left(\sigma_{xx}^{\infty}+\sigma_{yy}^{\infty}\right)\left(1-\frac{r_w^{\,2}}{r^2}\right)+\frac{1}{2}\left(\sigma_{xx}^{\infty}-\sigma_{yy}^{\infty}\right)\left(1-\frac{4r_w^{\,2}}{r^2}+\frac{3r_w^{\,4}}{r^4}\right)\cos 2\theta \\
&\quad+\sigma_{xy}^{\infty}\left(1-\frac{4r_w^{\,2}}{r^2}+\frac{3r_w^{\,4}}{r^4}\right)\sin 2\theta+p_R\frac{r_w^{\,2}}{r^2} \\
\sigma_\theta &= \frac{1}{2}\left(\sigma_{xx}^{\infty}+\sigma_{yy}^{\infty}\right)\left(1+\frac{r_w^{\,2}}{r^2}\right)-\frac{1}{2}\left(\sigma_{xx}^{\infty}-\sigma_{yy}^{\infty}\right)\left(1+\frac{3r_w^{\,4}}{r^4}\right)\cos 2\theta \\
&\quad-\sigma_{xy}^{\infty}\left(1+\frac{3r_w^{\,2}}{r^2}\right)\sin 2\theta-p_R\frac{r_w^{\,2}}{r^2} \\
\sigma_z &= \sigma_{zz}^{\infty}-2\nu\left[\left(\sigma_{xx}^{\infty}-\sigma_{yy}^{\infty}\right)\frac{r_w^{\,2}}{r^2}\cos 2\theta+2\sigma_{xy}^{\infty}\sin 2\theta\frac{r_w^{\,2}}{r^2}\right] \\
\sigma_{r\theta} &= -\frac{1}{2}\left(\sigma_{xx}^{\infty}-\sigma_{yy}^{\infty}\right)\left(1+\frac{2r_w^{\,2}}{r^2}-\frac{3r_w^{\,4}}{r^4}\right)\sin 2\theta+\sigma_{xy}^{\infty}\left(1+\frac{2r_w^{\,2}}{r^2}-\frac{3r_w^{\,4}}{r^4}\right)\cos 2\theta \\
\sigma_{rz} &= \left(1-\frac{r_w^{\,2}}{r^2}\right)\left(\sigma_{xz}^{\infty}\cos\theta+\sigma_{yz}^{\infty}\sin\theta\right) \\
\sigma_{\theta z} &= \left(1+\frac{r_w^{\,2}}{r^2}\right)\left(-\sigma_{xz}^{\infty}\sin\theta+\sigma_{yz}^{\infty}\cos\theta\right)
\end{aligned}
\tag{1}
$$

In Eq. 1, all stress components are effective stresses, including pressure (i.e., they are the actual stresses/pressure subtracted by initial pore pressure p_0). The stresses with superscript ∞ are the projected components of the remote in-situ stresses to the (x, y, z) coordinate system with z-axis aligned with the wellbore axis and x-axis lying in the plane orthogonal to the well axis and aligned with the high side of the wellbore, and r and θ are the corresponding polar coordinates in the (x, y) plane, as shown in Fig. 2. The p_R is the pressure applied at the rock face at the borehole wall. The stresses are those existing in the rock before casing is cemented in place. When a casing is cemented in the borehole, the effective wellbore pressure is approximately equal to the hydrostatic pressure of the cement column p_c. The actual pressure, or more accurately the radial stress applied at the interface between cement and rock interface, can evolve with time due to cement expansion/shrinkage due to chemical reaction and temperature changes as the cement cures and possibly also rock creeping. For simplicity, these effects are neglected here, and the stresses induced from the cement pressure are assumed to be permanently locked in once cement is set.

When fluid is pumped into the well after it is cased and perforated, the fluid pressure p_w is applied inside the casing. This pressure acting radially on the inside of the casing wall is only partially transmitted to the rock face since the casing is much stiffer than the rock. Li (1991) derived the radial stress transmitted to the interface of casing and cement and it is given as follows:

$$p_R == TF\ p_w \frac{R_o^{\ 2}}{r_w^{\ 2}}$$

$$TF = \frac{\frac{1+\nu_s}{E_s}\frac{2(1-\nu_s)}{R_o^{\ 2}-R_i^{\ 2}}R_i^{\ 2}}{\frac{1+\nu}{E}+\frac{1+\nu_s}{E_s}\frac{R_i^{\ 2}+(1-2\nu_s)R_o^{\ 2}}{R_o^{\ 2}-R_i^{\ 2}}} \quad (2)$$

where E_s and ν_s are Young's modulus and Poisson's ratio of the steel, and TF is the transmission factor defined as a fraction of the wellbore pressure transmitted as a radial stress on to the rock face.

The above calculation assumes the cement is perfectly bonded. If the bonding between the cement and casing or cement and rock is weak, fluid may penetrate the micro-annulus, resulting in an effectively higher fluid pressure applied at the rock face. However, in a high-rate pumping situation in the field, pressure rises rapidly, and there is short time for fluid to penetrate a significant distance along the casing/cement interface unless an open channel already exists. This is different from most laboratory conditions in which annulus penetration is often observed in that the laboratory fracturing tests are typically conducted at very low rate, and it takes a very long time to reach breakdown pressure, allowing ample time for fluid to seep into the annulus. It is also different from the later time when the fracture becomes much larger and causes the rock to detach from the casing as fracture width widens. Therefore, the perfect bonding is considered a reasonable assumption. The limiting case of very poor cement can also be assessed by setting TF to 1, in which case the wellbore pressure is directly applied at the rock face.

Along a perforation tunnel, the rock is subjected to varying circumferential stress σ_θ (also referred to as the "hoop stress"), axial stress σ_z, and radial and shear stresses, as a function of radial distance and angle, as indicated in Eq. 1. These stresses act as remote stresses on the perforation tunnel, causing further stress concentration in the rock around the perforation tunnel. Using the approximation as proposed by Hossain et al. (2000), the stress around the perforation tunnel can also be calculated using the same Kirsch equations.

This computation procedure is as illustrated in Fig. 3 at the base of the perforation. The initial stresses before perforating are computed from Eq. 1 by letting $r = r_w$ and $\theta = \theta_p$, which denotes the angle of the perforation. The resulting axial, tangential, and shear stresses acting on the perforation tunnel are σ_z, σ_θ, and $\sigma_{\theta z}$. From these stresses, the principal stresses σ_1 and σ_2 can be computed, as well as their angles.

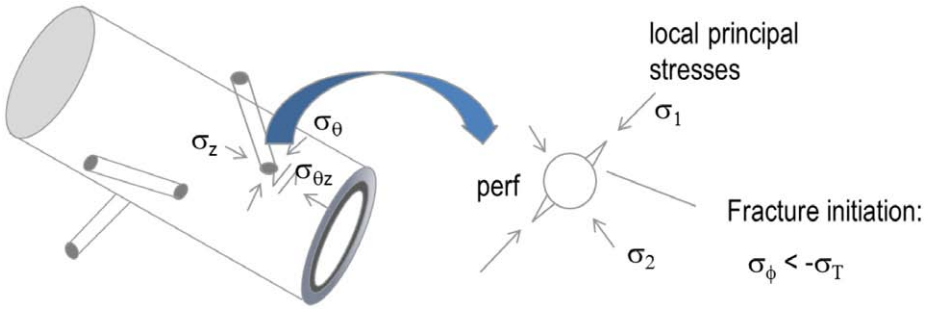

Figure 3—Diagram illustrating the stresses acting at the base of a perforation.

When the wellbore is pressurized, the perforation tunnel is exposed to the wellbore pressure p_w. As p_w increases, it induces an increasing tensile hoop stress around the perforation tunnel. At a sufficiently high p_w, the maximum tangential stress at the perforation wall, σ_ϕ, where ϕ refers to the angle around the circumference of the perforation tunnel, exceeds the tensile strength of the rock, σ_T, and a fracture initiates. That is, the fracture initiation pressure can be determined from the Hubert and Willis (1957) equation:

$$\sigma_\phi = 3\sigma_1 - \sigma_2 - p_w = -\sigma_T \quad (3)$$

where σ_1 is the smaller of the two principal stresses acting in the cross-sectional plane of the perforation tunnel.

A similar initiation pressure can be computed near the tip of the perforation tunnel. Due to the further distance from the borehole wall and the decay of the hoop stresses with radial distance, the stresses acting on the perforation tunnel approach the in-situ stresses. Depending on the in-situ stresses, well and perforation orientations and perforation length, the initiation pressure from the tip can be either higher or lower than that at the base of the perforation. The one with a lower value dictates whether the fracture will initiate from the base or tip of the perforation. For more detailed stress analyses and the expressions for the initiation pressure for wellbore orientations aligned with the in-situ principal stresses, please refer to Waters and Weng (2016).

Effect of Plasticity

The fracture initiation model presented in the previous section is based on the elasticity solution. However, when the remote compressive stresses acting on an open hole is sufficiently high, the rock at the borehole wall may yield under high compressive hoop stress. This could be the case around the borehole wall as soon as the well is drilled and is even more likely to occur around the perforation tunnels, which can be subjected to greater compressive stresses due to the hoop stress at the wellbore wall.

According to the elasticity solution, a remote compressive stress acting on an open hole creates a compressive hoop stress three times as large at the sides of the hole perpendicular to the stress while also creating a tensile hoop stress of the equal amount on the sides of the hole along the line of the applied stress. For a borehole subjected to the maximum and minimum principal stresses σ_1 and σ_2 in the plane perpendicular to the borehole, the rock on the borehole wall tangent to the maximum remote stress (point A in Fig. 4) is subjected to the largest compressive hoop stress:

$$\sigma_{\theta\max} = 3\sigma_1 - \sigma_2 \quad (4)$$

The positions on the borehole wall that have the least compressive stress are those tangent to σ_2 (point B in Fig. 4), with

$$\sigma_{\theta\min} = 3\sigma_2 - \sigma_1 \quad (5)$$

If $\sigma_{\theta\max}$ is greater than the uniaxial compressive strength (UCS) of the rock, the rock at the point A will undergo plastic deformation, or breakout.

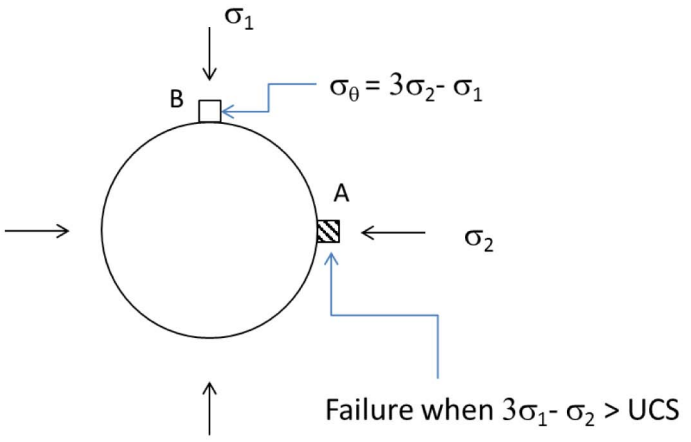

Figure 4—Diagram showing the yielding or breakout at borehole wall (point A) when the maximum compressive hoop stress exceeds UCS; position at 90° from the breakout (point B) has the least compressive stress and is where fracture will initiate when later subjected to internal pressurization.

It has been observed in laboratory block experiments (Cook 2008) that the initiation pressure increases above the theoretical initiation pressure when the theoretical maximum hoop stress exceeds the UCS. The experiments were carried out in sandstone and shale cubic blocks of 150-mm size with a 25-mm borehole, subjected to anisotropic confining stresses. Experiments were carried out to test the onset of fracturing to cause loss of circulation when injecting different drilling fluids with or without filter cake formation. Comparison of the measured fracture initiation pressure is made with the theoretical initiation pressure based on the elastic solution as given by Eq. 3. Many of the tests were conducted with a large difference between the two principal stresses. From the sandstone tests, it was found that the measured initiation pressure agrees well with the elastic solution for tests where the maximum hoop stress was below the rock yield stress, but the measured initiation pressure was greater than that predicted from the elasticity solution when the theoretical (elastic) maximum hoop stress exceeded the yield stress. Fig. 5 shows the experimental data for the tests using Grinshill sandstone.

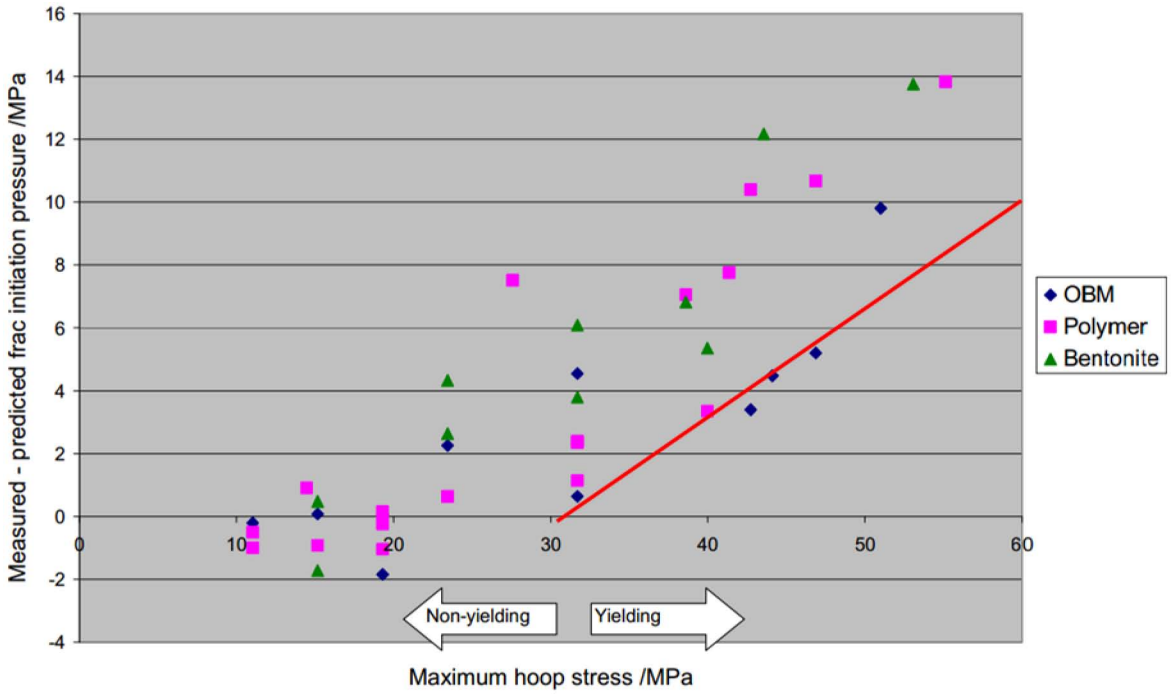

Figure 5—Difference between the measured and predicted fracture initiation pressures vs. the maximum hoop stress based on the elasticity theory – sandstone block tests (Cook, 2008). The red line is the proposed correlation to the elastic initiation pressure (Eq. 6).

Fig. 5 shows that the difference between the measured and the predicted initiation pressure is small when the theoretical maximum hoop stress at the borehole wall is below 20 MPa. The error starts to increase when the maximum hoop stress exceeds the unconfined yield stress of the rock (representative of the condition at the borehole wall) of approximately 30 MPa and increases linearly as the nominal maximum hoop stress increases.

The experimental data suggest that to more accurately predict the fracture initiation pressure, especially where the applied remote stresses are large, the rock yielding effect must be considered. The hoop stress at the borehole wall is even more magnified if the two remote stresses are significantly different which is evident from Eq. 4. This is certainly the case for fracture initiation from perforations, which are often subjected to very different principal stresses at the borehole wall due to the local stress concentration.

The experimental data indicate that the discrepancy of the measured and the theoretical initiation pressure based on the elasticity increases approximately linearly with the maximum hoop stress as it exceeds the UCS. The mechanism for this discrepancy is still not well understood, nor is a model for its prediction. At

present, we incorporate in the initiation model a correction as given in Eq. 6. Further research is needed to fully understand the effect of borehole yield on subsequent fracture initiation.

$$\Delta p_{\text{init}} = (3\sigma_1 - \sigma_2 - \text{UCS})/3 \tag{6}$$

This correction is shown as the red line in Fig. 5.

It should be noted that the correction adopted here is only intended for "moderate" yielding at the perforation wall. If the compressive stresses are sufficiently large that the entire circumference of the perforation tunnel is yielded, then the perforation tunnel would likely collapse, such that the fracture will either not be able to initiate or have severe restriction for the fluid to enter. Furthermore, this correction is only applied to the perforation hole. The hoop stress around the wellbore is still computed based on the Kirsch elasticity solution, as given in Eq. 1. One reason for this assumption is that the difference between the principal stresses acting on the perforation can be much greater than those acting on the wellbore and hence plastic yield is far more likely to occur at the perforation wall. Second, the exact solution of the hoop stress as a function of hole angle and distance is not available if yielding occurs, which is needed to compute the stresses acting on the perforation. If severe yielding already occurs around the borehole before perforating, the analytical model is not applicable and numerical simulation will be required for more accurate modeling.

Model Validation

Validation against Numerical Simulation

Alekseenko et al. (2012) presented numerical simulation results for a series of cases for fracture initiation from a perforated, uncemented borehole using a 3D boundary element code. For validation purposes, the results from the analytical model described above are compared to the Alekseenko et al. numerical results for a series of sensitivity cases presented in their paper.

Fig. 6 shows the geometry of a horizontal wellbore and the remote stresses for the case of a single perforation connected to an open borehole in the parametric study by Alekseenko et al. (2012). The wellbore is oriented parallel to the minimum horizontal stress σ_h.

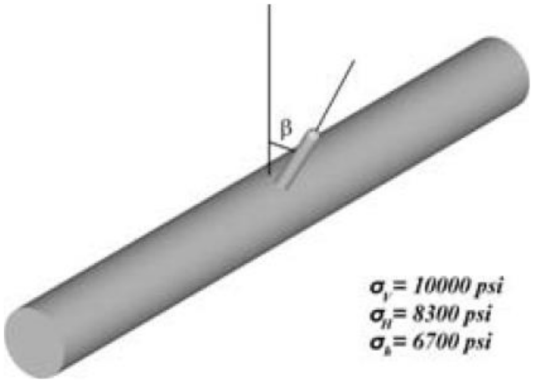

Figure 6—Schematic of the simulated perforation geometry by Alekseenko et al (2012).

Fig. 7 shows the computed fracture initiation pressure as a function of the perforation angle for different values of maximum horizontal stress $\sigma_{h\max}$, with the numerical simulation results by Alekseenko et al. shown in Fig. 7a, and that from the current analytical model shown in Fig. 7b. For the smaller values of $\sigma_{h\max}$, the initiation pressure increases as the perforation orientation (with respect to the wellbore top position) increases. At a perforation angle of approximately 50°, the initiation pressure from the perforation exceeds the initiation pressure of a longitudinal fracture from the borehole wall. Therefore, the plateau shown in Fig. 7 at angles greater than 50° corresponds to the fracture initiation from the borehole wall.

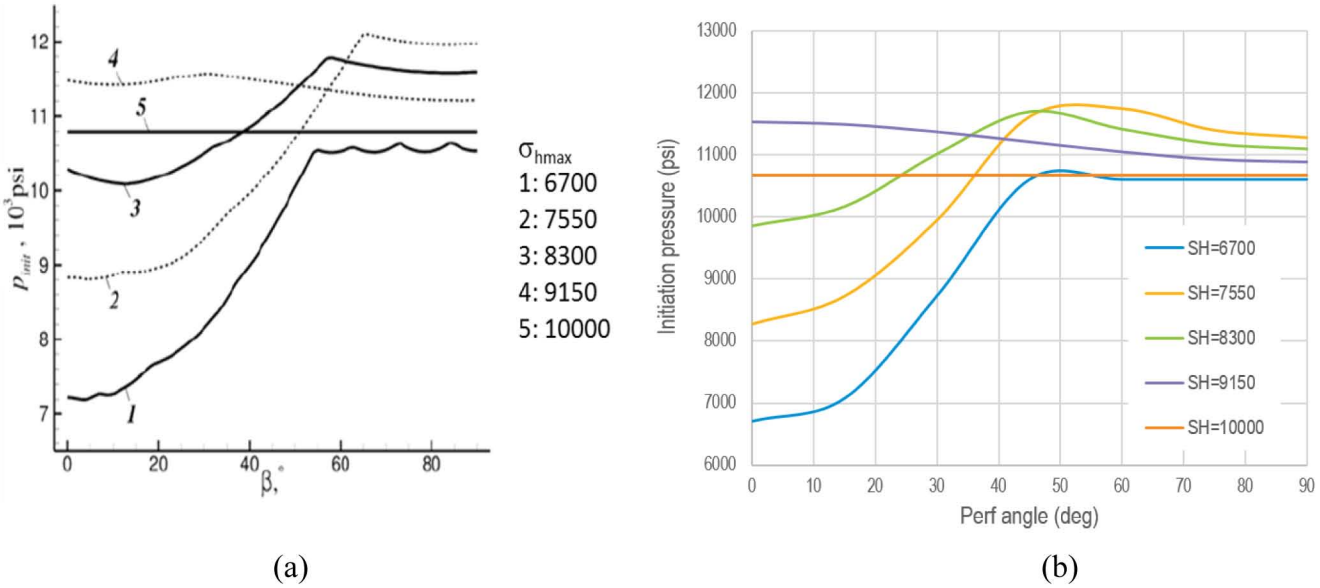

Figure 7—Variation of fracture initiation pressure as a function of the perforation angle at varying maximum horizontal stress: (a) from numerical simulations by Alekseenko et al. (2012); (b) results from the analytical model.

The fracture initiation pressure predicted by the analytical model, shown in Fig. 7b agrees reasonably well with the numerical simulation results (Fig. 7a).

Comparison to Laboratory Experiments

The experiments for fracture initiation from a cased and perforated configuration are relatively few in the literature. Analyses of the pressure response in the block experiments are also complicated by the facts that highly viscous fluids are typically used for proper scaling of slow injection in the laboratory to the field pumping conditions based on the fracture propagation considerations (rather than fracture initiation) as well as large storage effect in the experimental setup, which can cause significant fluid friction in the fracture entrance and much higher "breakdown" pressure than the initiation pressure (see, e.g., Lecampion 2012; Lecampion et al. 2015; van der Ketterij and de Pater, 1997). Additional complication arises since most laboratory block experiments were done on samples with casing cemented before applying the loads, rather than cemented under stresses which is more representative of the conditions in the field (Behrmann and Elbel 1991).

Behrmann and Elbel (1991) presented a series of large block experiments in which a 3.5-in. outside diameter (OD) steel tubing [2.5-in. inside diameter (ID)] was cemented in a 4.5-in. borehole drilled in a sandstone block (27 in. × 27 in. × 32 in.) and perforated with actual perforating shape charges. The blocks were subjected to triaxial stresses with $\sigma_{h\min}$ = 3180 psi, $\sigma_{h\max}$ = 4100 psi. Hydraulic fractures were created by injecting brine or glycerin into the borehole until the fracture propagates to the block boundary. The injection pressure and confining stresses were recorded. Two different rocks were used in their experiments, Torrey Buff Sandstone and Gold Sandstone. The former has a permeability of 0.49 md and compressive strength of 5870 psi (parallel to bedding) and the latter 164 md and 4080 psi. Table 1 lists the vertical well experiments with the measured breakdown pressures and the fracture initiation pressures predicted from the current analytical model at the base and tip of the perforations. Test 2 in Behrmann and Elbel (1991) is excluded from this analysis due to the complication of initial injection rate being too low and six injection cycles required to initiate the fracture; the single horizontal well test is also excluded in the following analyses. A rock tensile strength of 500 psi is assumed in these calculations.

Using a dimensionless parameter $\sum$ as defined by Lecampion et al. (2015) to assess the intensity of the viscous effect, it is estimated to be in the order of 1.0×10^{-3} for the brine tests, which indicates

negligible viscous effect, and approximately 30 for the glycerin tests, which suggests appreciable viscous effect. However, the measured breakdown pressure in the experiments as shown in Table 1 does not show significant difference between the brine and glycerin tests.

Table 1—Block experiments with vertical cased and perforated borehole by Behrmann and Elbel (1991) and comparison of the actual breakdown pressure vs. predicted initiation pressure.

Test	Rock	Perf angle from σ_{hmin}	Perf length (in.)	Fluid	σ_v (psi)	P_0 (psi)	Measured P_{brdn} (psi)	Location	Predicted P_{init} (psi) – Open hole	Predicted P_{init} (psi) – Perf tip	Predicted P_{init} (psi) – Perf base
3	Torrey Buff	60°, 60°	6.8, 8.0	Glycerin	6370	0	5650	Annulus	5940	6186	6868
4	Torrey Buff	60°, 240°, 60°	6.8, 3.1, 6.4	Brine	6370	0	5550	Base of perfs	5940	6096	6384
5	Gold	60°, 240°, 60°, 240°	4, 4.9, 6, 5.8	Glycerin	6370	2000	6500	Base of perfs	3940	4744	6220
6	Gold	30°, 210°, 30°, 210°	5.5, 4.6, 6.7, 3.3	Glycerin	6370	2000	7000	Annulus	3940	5916	6576
7	Torrey Buff	60°, 240°, 60°, 240°	5.9, 5.7, 5.9, 3.8	Brine	5460	2000	7600	Perf base & annulus	3940	4682	6144
8	Torrey Buff	60°, 240°, 60°, 240°	5.5, 3.1, 4.9, 4.6	Brine	5460	2000	6000	Base of perfs	3940	4698	6144
9	Torrey Buff	80°, 260°, 80°, 260°	4.1, 3.7, 5.9, 3.4	Brine	5460	2000	6600	Base of perfs	3940	4456	4447

As can be seen in Table 1, for tests 3 and 4 with perforations misaligned by 30° from the preferred fracture plane (90° from σ_{hmin}) and no initial pore pressure, the predicted initiation pressure for open hole (without perforation) and that for the cased hole with perforations, both from the tip and the base of the perforations, are quite close. Therefore, fracture initiation from the annulus is possible if the cement bonding is poor. Fracture initiation from both the base of the perforations and the cement annulus were observed in these tests. The predicted initiation pressures agree reasonably well with the measured breakdown pressures.

For tests 5–9, with the blocks initially saturated and an applied pore pressure of 2000 psi, the predicted initiation pressure for the vertical open hole, based on the Hubert and Willis equation, is significantly below the actual breakdown pressure. The initiation pressures for the cased and perforated wellbore show lower initiation pressures at the tip of the perforation than at the base of the perforation, which therefore suggest that initiation from the perforation tips is more likely. The relatively low predicted initiation pressure at the tip is a result of the large contrast between the vertical stress and minimum horizontal stress. As a reference point, if one considers a perforation aligned with fracture plane as an open hole and at a location far enough away from the influence of the hoop stress around the wellbore, the Hubert and Willis equation based on the elasticity would give an initiation pressure of 1670 psi for tests 5 and 6, and 2580 psi for tests 7–9, which imply the fracture would initiate even before the wellbore pressure reaches the minimum in-situ stress. The correction of the plasticity effect based on the discussion in the previous section results in higher tip initiation pressures shown in Table 1 than Hubert and Willis. However, they are still considerably lower than the actual measured breakdown pressure. The observations by Behrmann and Elbel from these experiments indicated that the fractures mostly initiated from the base of the perforations, contradicting the expected tip initiation based on the computed initiation pressures. Since the compressive strengths of the rocks are relatively low (5870 and 4080 psi for Terrey Buff and Gold Sandstone, respectively) as compared to the applied stresses, such that the hoop stress around the perforation tunnel (or even the main borehole for Gold Sandstone) far exceeds the UCS of the rock, it is quite possible that fracture did not initiate from the tips of the perforations due to rock failure, perforation tunnel collapse, or debris blocking the tunnels.

If we constrain the fracture initiation only from the base of the perforation, the computed initiation pressures agree well with the measured breakdown pressure, as shown in Table 2, with the exception of

test 9 in which the perforations misaligned with the expected fracture plane by only 10°. With perforation nearly aligned with the fracture plane, the predicted initiation pressure is lower than the other tests (30° misalignment) as one would expect. However, the measured breakdown pressure in the experiment in this test was similar to that in the other tests. One possible explanation for the higher pressure is the large pore pressure increase in the block by more than 1500 psi as measured by the pore pressure probe in this test before the breakdown even occurs (see Behrmann and Elbel 1991), which would most likely have resulted in drastic increase of the total stresses applied on the block in the experimental setup.

The above example showed some of the challenges in predicting the fracture initiation pressure. Large discrepancy may exist between the prediction based on the elastic theory and the actual initiation pressure, especially if the rock is subjected to high hoop stress far exceeding its compressive strength, either around the perforation tunnel or wellbore. Although the current model with empirical correction improves the prediction over the elastic model, the model still needs to be applied judiciously to sufficiently competent rocks under in-situ conditions. Despite the current limitations, the initiation model can provide a useful tool for assessing the fracture initiation from the cased and perforated completion and the effectiveness in creating fractures in multiclustered perforations.

Field Case Study

To better understand the best approach to drill, complete, and produce a new horizontal well that minimizes any environmental/social costs while maximizing economic productivity, an Appalachian basin shale gas study was conducted in a Marcellus shale horizontal test well located near Morgantown in Monongalia County, West Virginia. This study was sponsored by the DOE's National Energy Technology Laboratory, and its partners, West Virginia University, The Ohio State University, and Marcellus shale operator Northeast Natural Energy under the MSEEL consortium (Anifowoshe et al. 2016).

The pilot hole was drilled and logged with advanced logging suites for reservoir evaluation. A multimineral lithology model was built with triple-combo and spectroscopy data. The pore size distribution was analyzed with the magnetic resonance data. Intervals with best reservoir quality were used to guide the lateral landing point. The target for the lateral is slightly above the Cherry Valley limestone which overlies the Lower Marcellus. The average TOC is 13%, the average effective porosity is 7%, and the T2 distribution is slightly shifted toward longer T2 than the Lower Marcellus indicating some larger pores (Anifowoshe et al. 2016). The maximum horizontal stress direction is N57°E based on the drilling induced fractures from the pilot hole and it is in alignment with the microseismic data after the lateral was completed (Wilson et al. 2016; Carr et al. 2017).

Based on the pilot hole evaluation program, the lateral was drilled in the minimum horizontal stress direction and geosteered with gamma ray. The completion quality along the lateral was evaluated with acoustic and image data (Fig. 8). The image logs identified over 1600 natural fractures with varying fracture intensity along the lateral. The majority of these natural fractures strike N78°E, with the fracture intensity (P32) of up to 4 fractures per foot. Geomechanical properties including the rock elastic properties and in-situ stresses were evaluated using the dipole sonic data. The anisotropic elastic mechanical properties along the different orientations parallel and perpendicular to the bedding are highly influenced by the formation laminations. These properties were estimated using a MANNIE rock physics model (Schoenberg et al. 1996; Suarez and Bratton 2009). The horizontal stresses were computed using two static poroelastic horizontal strain equations which relate the effective stresses to the static moduli and lateral tectonic strains (Higgins et al. 2008).

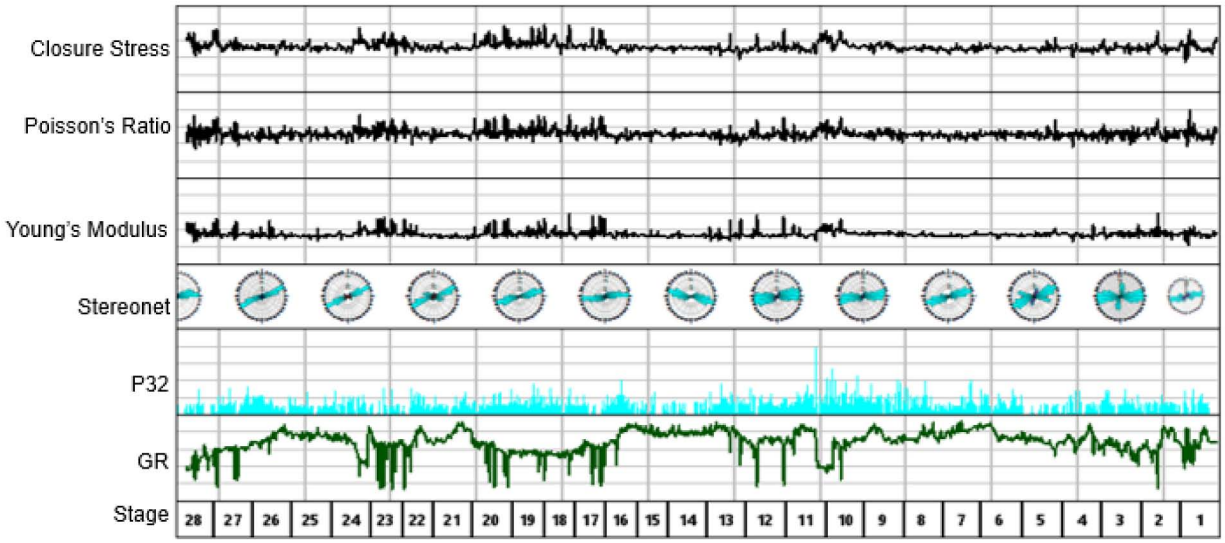

Figure 8—Lateral data. Curves are as follows (bottom-top): gamma ray, natural fracture intensity (P32), fracture stereonet, Young's Modulus, Poisson's Ratio, and minimum horizontal stress.

The horizontal test well was completed in 28 stages and stimulated with hydraulic fractures. Fiber optic cable was deployed for diagnostics using distributed temperature survey (DTS) and distributed acoustic sensing (DAS) technologies. To prevent damage to the fiber optic cable, the perforations were shot in zero-degree phasing (shown in blue in Fig. 9) away from the blast protectors (shown in red in Fig. 9). Table 2 summarizes the detailed formation and completion information for all the stages.

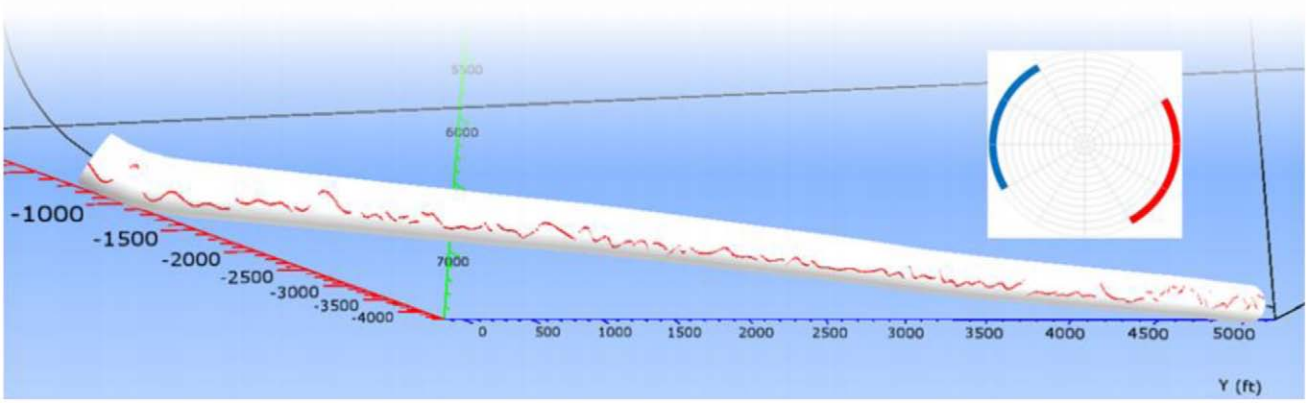

Figure 9—Perforation orientation away from the blast protectors of the fiber optic cable shown in red (Anifowoshe et al. 2016).

Table 2—Summary of stage information and initial breakdown

Stage	No. of clusters	Bottom cluster (ft)	Total shots	Lowest σ_h (psi)	Lowest σ_H (psi)	σ_v (psi)	Bkdn rate (bpm)	Measured P_{brdn} (psi) - surface	Predicted P_{brdn} (psi) - surface
1	5	13,809	50	6827	7050	8676	15.8	6946	5240
2	5	13,576	50	7421	7712	8676	15	6331	6634
3	5	13,353	50	7244	7518	8675	15.5	6770	6300
4	5	13,118	50	7391	7654	8684	15.4	6246	5922
5	5	12,884	50	7435	7706	8691	15.5	6208	6740
6	5	12,650	50	7521	7786	8694	15.4	5994	6721
7	5	12,418	50	7395	7655	8697	15	6580	6526
8	5	12,194	50	7554	7828	8707	15	6440	7022
9	5	11,971	50	7489	7774	8708	15.7	6498	6876
10	5	11,735	50	7618	7894	8712	15.1	6784	7094
11	5	11,509	50	7271	7544	8714	15.8	6322	6173
12	5	11,277	50	7370	7634	8711	14	6049	6514
13	5	11,046	30	7324	7585	8710	14	6300	6343
14	5	10,822	30	7388	7652	8711	15.2	6905	6587
15	4	10,594	26	7473	7740	8711	15.1	7115	6791
16	4	10,408	26	7107	7424	8711	15.5	7156	5980
17	4	10,139	32	7712	7984	8710	15.2	7950	6879
18	4	10,048	32	7748	8018	8710	15	6616	7476
19	4	9,869	32	7508	7778	8713	15.3	6062	6824
20	5	9,685	40	7508	7769	8720	15	6319	6023
21	5	9,445	40	7472	7731	8725	15	6506	6709
22	5	9,227	40	7423	7682	8730	15.2	6836	6562
23	5	9,005	40	7624	7913	8735	15	7562	7081
24	5	8,763	30	7392	7611	8741	15	6373	6433
25	5	8,541	32	7433	7695	8745	15	6628	6540
26	5	8,310	40	7457	7742	8753	15.5	6807	6625
27	4	8,085	40	7666	7925	8756	15.6	6895	7139
28	4	7,901	40	7718	8010	8752	15.3	7185	7317

Table 2 and Fig. 10 show the comparison of the measured breakdown pressure for all stages and the predicted breakdown pressure using the analytical fracture initiation model using the in-situ stresses derived from the sonic logs and the 1D geomechanical model. The predicted breakdown pressure at surface is computed from the bottomhole breakdown pressure from the model by subtracting the hydrostatic pressure and adding fluid friction pressure, which is estimated based on the instantaneous pressure drop at the shut-in from the recorded treating pressure. Table 2 also lists the lowest stresses among the clusters in each stage as a reference. Within each stage, despite the attempt to perforate at locations with similar minimum stress, there is still appreciable variation in the stresses from cluster to cluster.

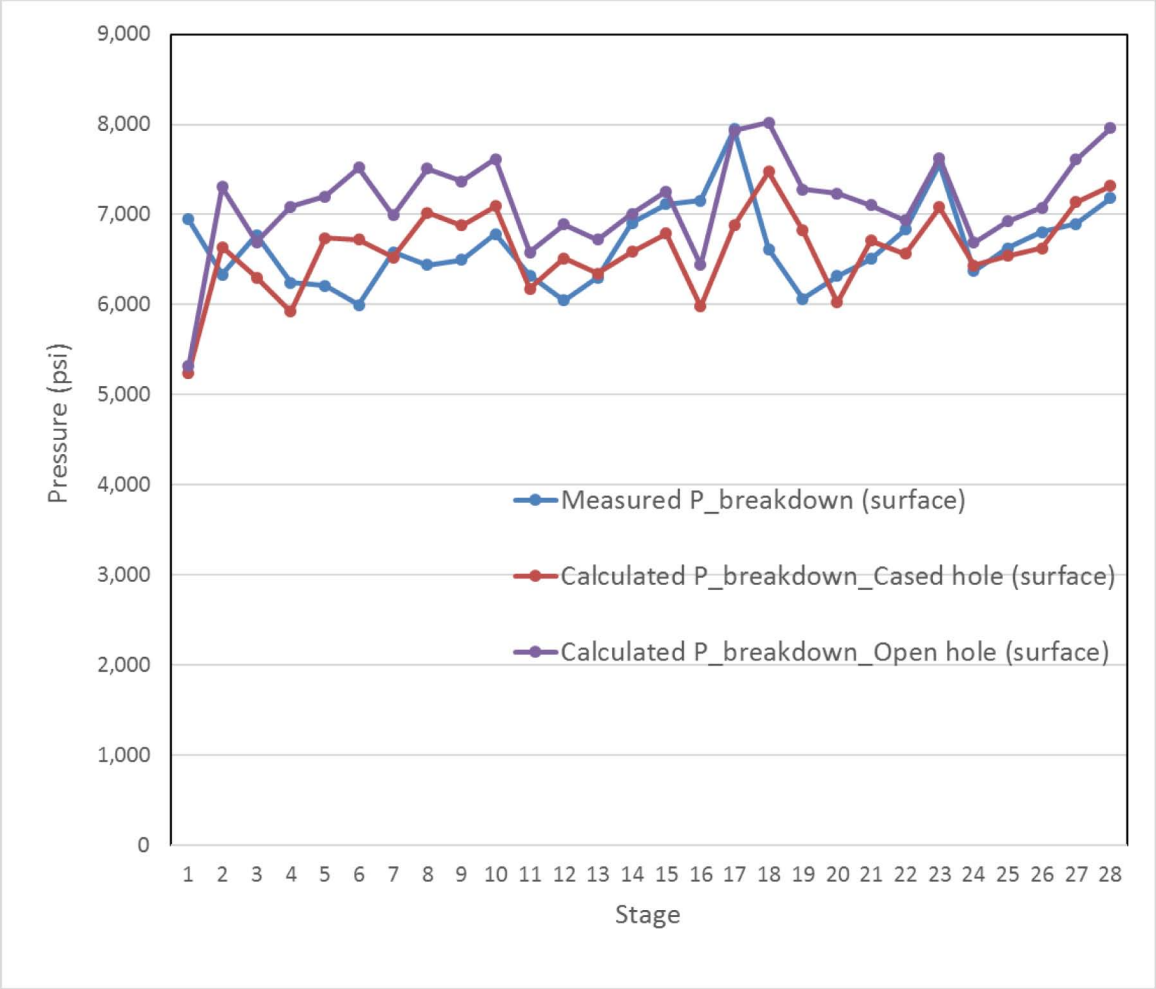

Figure 10—Comparison of measured and the predicted breakdown pressures.

The rock UCS was also estimated based on the log. An average value of 8000 psi is used in the fracture initiation calculation. For comparison, Fig. 10 also shows the predicted fracture initiation pressure for an open hole, which is higher than the initiation pressure from perforations. The trend of the variation of the predicted perforation breakdown pressure from stage to stage generally agrees with the measured breakdown pressure although there are some discrepancies for a few stages. The calculated breakdown pressure closely follows the trend of the minimum horizontal stress. These discrepancies could be attributed to the uncertainty in the sonic derived in-situ stresses, perforation orientation, and other parameters.

The initial "breakdowns" as shown in Table 2 were conducted at a relatively low pump rate when a ball is pumped down to activate the isolation plug. For the main fracturing treatment, the pump rates were increased drastically to 80 to 100 bbl/min, which significantly increased the treating pressure and hence further breaking down additional perforations which might have not broken down in the initial low rate breakdown stage. Fig. 11 shows the treating rate and surface pressure for one of the stages as an example.

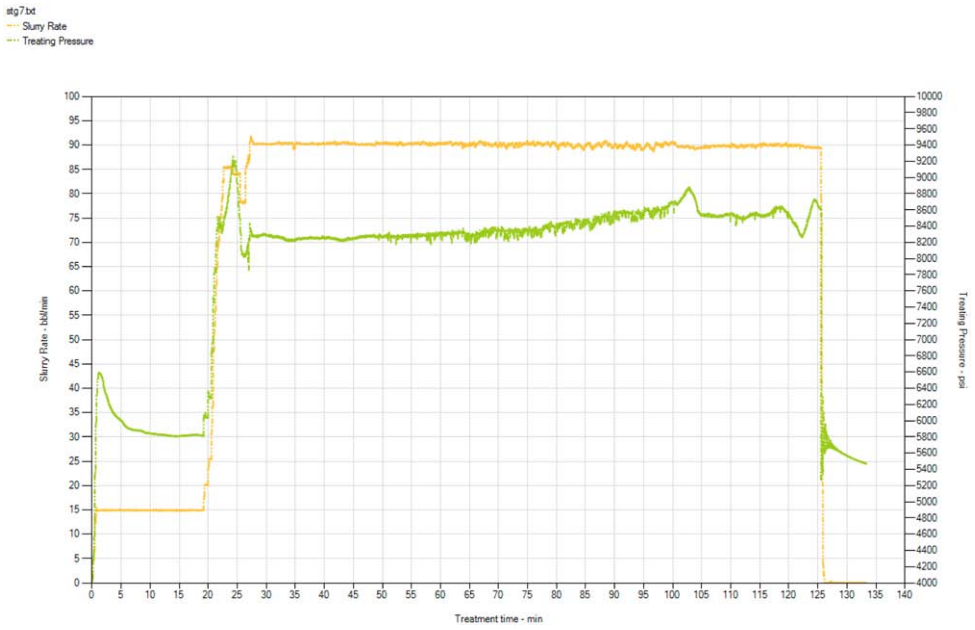

Figure 11—Example of the treating rate and pressure (stage 7).

The computed breakdown pressure for each stage and the number of perforations broken down at the main treatment rate are shown in Table 3, and the initiation pressure for all the perforation clusters are shown in Fig. 12.

Table 3—Summary of stage breakdown pressure and number of perforation clusters broken down.

Stage	No. of clusters	Total shots	Maximum pump rate (bpm)	Predicted Pbrdn (psi) - bottomhole	No. of clusters broken down
1	5	50	91	10119	3
2	5	50	91	10133	3
3	5	50	90	9759	3
4	5	50	91	10021	3
5	5	50	89	10213	3
6	5	50	91	9873	3
7	5	50	92	9553	3
8	5	50	100	10213	3
9	5	50	100	10403	3
10	5	50	101	11098	3
11	5	50	100	10418	3
12	5	50	100	9928	3
13	5	30	97	9946	5
14	5	30	100	10258	5
15	4	26	80	10530	4
16	4	26	81	10400	4
17	4	32	80	10367	3
18	4	32	94	10964	4
19	4	32	100	11281	3
20	5	40	100	10383	4
21	5	40	100	10055	4
22	5	40	100	10764	4
23	5	40	100	12218	3
24	5	30	100	10242	5
25	5	32	100	10355	5
26	5	40	100	10239	4
27	4	40	100	10483	3
28	4	40	96	11652	4

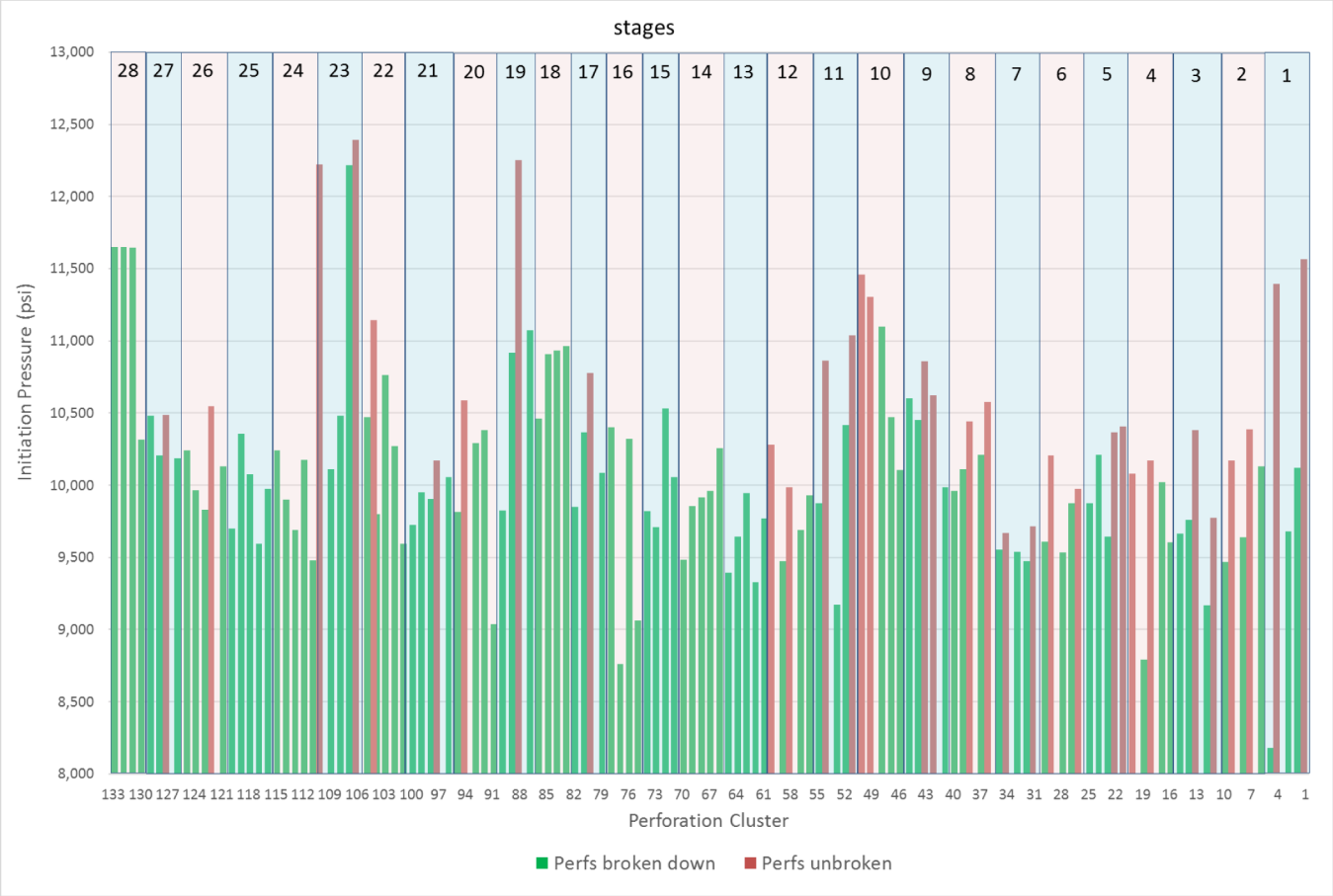

Figure 12—Predicted fracture initiation pressure for all the perforations.

Table 3 and Fig. 12 show that not all perforation clusters are broken down for many stages. For stages 1 to 12, with larger number of perforations (five clusters with 10 perforations per cluster), only three out of five clusters are predicted to be broken down. From stage 13 to 16, with more limited number of perforations (six perforations per cluster), all clusters are predicted to be broken down. And for the rest of the stages, with moderate number of perforations (around eight perforations per cluster), the result is mixed with varying degree of breakdown efficiency.

Discussion

Fig. 13 shows a summary of the cluster performance score based on the interpretation of the DAS measurement from the fiber optic sensor by Anifowoshe et al. (2016). The dark blue bars on the top plot represent the normalized total energy (cluster score) at each cluster. The green, yellow, and red bars below the horizontal axis denotes good, average, and poor cluster performance based on a predetermined cutoff value from the cluster score. The dark blue bars on the lower plot represent the standard deviation of the cluster score for each stage. Stages 1 to 12 with geometric completions and larger number of perforations have much greater variation in the cluster performance and, on average, lower cluster efficiency (indicated by the cluster performance score). The stages with the engineered perforation locations and limited entry design with reduced number of perforations have more uniform stimulation and on average higher cluster efficiency. The predicted cluster breakdown as shown in Fig. 12 shows a similar trend, even though the clusters predicted not broken down may not match exactly the DAS interpretation, which could again be due to the uncertainty in the derived in-situ stresses, perforation orientation, and other parameters.

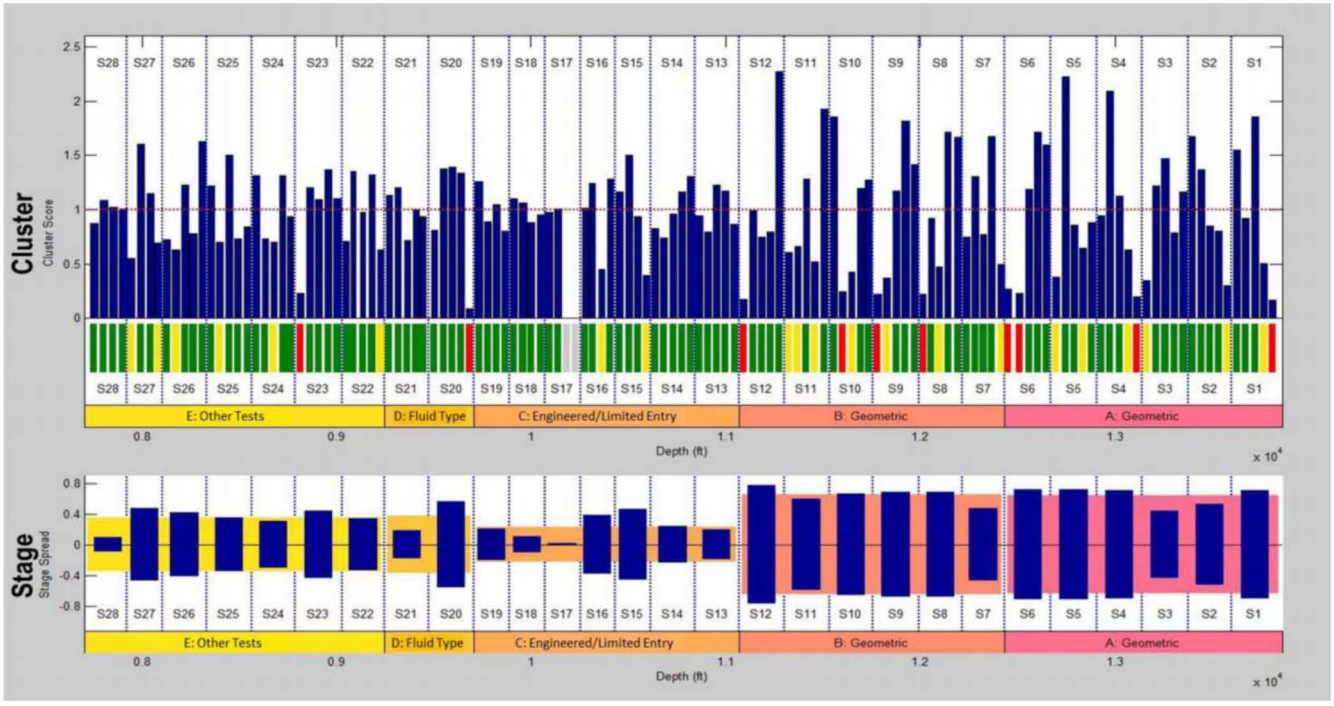

Figure 13—Summary of cluster, stage, and section performance interpretation based on the DAS data (Anifowoshe et al. 2016).

The lower cluster breakdown efficiency for the stages with a greater number of perforations as predicted by the model is due to the reduced perforation friction associated with a given flow rate through a perforation cluster. As the number of perforations increases, the given flow rate is distributed to more perforation holes, resulting in less entry friction pressure drop and hence less diversion force. Consider two perforation clusters with a given difference in fracture initiation pressure between the two, the cluster with the lower initiation pressure will be broken down first. If the perforations can accommodate the total pump rate through the open perforations without exceeding the initiation pressure of the second cluster (i.e., the propagation pressure plus perforation friction is below the initiation pressure), a fracture will not be initiated from the second cluster. Therefore, clusters with a larger number of perforations can each accommodate a greater flow rate before overcoming the given difference in initiation pressure to break down the next cluster, leading to less effective breakdown when multiple clusters are present.

Although the engineered perforation design reduces the stress difference among the clusters in each stage, which helps improve the breakdown efficiency, some of the perforation clusters are still possibly not broken down due to another driver for inefficient fracture initiation in the multiclustered completion, which is the difference between the fracture initiation pressure and the propagation pressure. When there is a large difference between the initiation pressure and the minimum in-situ stress, a larger diversion force (i.e., more limited-entry perforation design) is required to break down all the perforation clusters. Otherwise, after a few clusters are broken down and the fractures start propagating, the bottomhole pressure will drop and not be able to maintain the required initiation pressure for the rest of the clusters.

The operational constraint of having to perforate zero-degree phasing in this well to avoid damaging the fiber optic cable may have also contributed to the problem of the inefficient perforation breakdown. In the more conventional spiral perforating, the perforations with different orientations have different initiation pressures. Therefore, when bottomhole pressure increases, perforations within a cluster are broken down sequentially at different pressures, and some with higher initiation pressure may not be broken down at all. This creates a greater perforation friction to drive the pressure up to break down the next clusters. In contrast, with zero-degree phased perforations, they have approximately the same initiation pressure. After the bottomhole pressure reaches the initiation pressure, all perforations in the cluster are broken down at the

same time, creating less diversion force compared to the spiral perforations. Furthermore, for zero-degree phased perforations, the fracture initiation pressure is strongly dependent on the perforation orientation. For a more favorable perforation orientation (usually top/bottom orientations for a horizontal well), the initiation pressure is much lower than a less favorably oriented perforation. Therefore, the perforation orientation variation from cluster to cluster introduces additional contribution to the variation in fracture initiation pressure, on top of the lateral variation in in-situ stresses, exacerbating the problem. In comparison, the commonly adopted 60° phased spiral perforating will always have at least one pair of perforations within 30° from the most favorable orientation and will most likely have less variation in the initiation pressure from cluster to cluster.

Conclusion

In this paper, an analytical fracture initiation model for a cased and perforated wellbore is presented along with the comparison against selected 3D numerical simulations and experimental data available in the literature. The model agrees well with the previous numerical simulation results. Comparison with the experimental data from the previous large block tests by Behrmann and Elbel (1991) showed mixed results, with the model showing lower fracture initiation pressure from the tips of the perforation tunnels whereas the experiments showed fracture initiation from the base of the perforations or micro-annulus in the tests. Due to the relatively large applied stresses and consequently large hoop stresses around the borehole and perforations that far exceeded the rock compressive strength, it is postulated that many of the perforation tunnels might have been severely damaged or collapsed, leading to fractures not being able to initiate from the perforation tips in these tests. If assuming the fractures do initiate from the perforation base, the model gives a reasonably good agreement with the experimental results. The comparison with the experimental data also highlighted rock yielding as a situation that may often occur, which compromises the more simplistic elastic analysis. Although an empirical correction based on limited experimental data is introduced in the current model presented in this paper to account for the effect of yielding on the initiation pressure, further research is needed to better understand and quantify the effect of rock yielding and plasticity on fracture initiation.

The paper also presented the fracture initiation and breakdown analysis using the data from a Marcellus horizontal test well in the DOE-sponsored MSEEL project. The model prediction suggests some of the stages with a larger number of perforations may have left some clusters not broken down. In contrast, some of the stages with a reduced number of perforations are predicted to have all clusters effectively broken down. The less-efficient breakdown of the clusters may also be exacerbated due to the operational constraint of having to perforate at zero-degree phasing in this test well to avoid damaging the fiber optic cable.

Acknowledgments

We would like to thank Schlumberger and Northeast Natural Energy LLC for permission to publish this paper. We want to thank Dr. John Cook for sharing the data on the previously unpublished block test results, and Olatunbosun Anifowoshe and Malcolm Yates for their prior work in collecting and analyzing the data from the field case study included in this paper. We also thank US Department of Energy National Energy Technology Laboratory and all the MSEEL consortium members for making the data available and permission to publish this study.

References

Abass, H.H., Hedayati, S., and Meadows, D.L. 1996. Nonplanar Fracture Propagation from a Horizontal Wellbore: Experimental Study. *SPE Prod & Fac* **11** (3): 133–137. SPE-24823-PA. https://doi.org/10.2118/24823-PA.

Alekseenko, O.P., Potapenko, D.I., Cherny, S.G., Esipov, D.V., Kuranakov, D.S. and Lapin, V.N. 2012. 3-D Modeling of Fracture Initiation from Perforated Non-Cemented Wellbore. Presented at the SPE Hydraulic Fracturing Technology Conference, The Woodlands, Texas, USA, 6–8 February. SPE-151585-MS. https://doi.org/10.2118/15185-MS.

Anifowoshe, O., Yates, M., Xu, L., Dickerson, P., Akin, J., Carney, B.J., Hewitt, J., Costello, I., and Arnold, Z. 2016. Improving Wellbore Stimulation Coverage in the Marcellus: Integrating Lateral Measurements with Enhanced Engineered Completion Design and Fiber Optic Evaluation. Presented at SPE Eastern Regional Meeting, Canton, Ohio, 13-15 September. SPE-184051-MS. https://doi.org/10.2118/184051-MS.

Behrmann, L.A. and Elbel, J.L. 1991. Effect of Perforations on Fracture Initiation. *J Pet Technol* **43** (5): 608–615. SPE-20661-PA. https://doi.org/10.2118/20661-PA.

Behrmann, L.A. and Nolte, K.G., 1998. Perforating Requirements for Fracture Stimulations. Presented at the SPE International Symposium on Formation Damage Control, Lafayette, Louisiana, USA, 18–19 February. SPE-39453-MS. https://doi.org/10.2118/39453-MS.

Carr, T. R., Wilson, T., Kavousi, P., Amini, S., Sharma, S., Hewitt, J., Costello, I., Carney, B.J., Jordon, E., Yates, M., MacPhail, K., Uschner, N., Thomas, M., Akin, J., Magbagbeola, O., Morales, A., Johansen, A., Hogarth, L., Anifowoshe, O., Naseem, K., Hammack, R., Kumar, A., Zorn, E., Vagnetti, R., and Crandall, D. 2017. Insights from the Marcellus Shale Energy and Environment Laboratory (MSEEL). URTEC-2017-2670437.

Cipolla, C., Weng, X., Onda, H., Nadaraja, T., Ganpuly, U. and Malpani, R. 2011. New Algorithms and Integrated Workflow for Tight Gas and Shale Completions. Presented at the SPE Annual Technical Conference and Exhibition, Denver, Colorado, USA, 30 October–2 November. SPE-146872-MS. https://doi.org/10.2118/146872-MS.

Cook, J. 2008. Personal communication.

El Rabaa, W. 1989. Experimental Study of Hydraulic Fracture Geometry Initiated from Horizontal Wells. Presented at the Annual Technical Conference and Exhibition, San Antonio, Texas, USA, 8–11. SPE-19720-MS. https://doi.org/10.2118/19720-MS.

Higgins, S. M., Goodwin, S. A., Donald, A., Bratton, T. R., and Tracy, G. W. 2008. Anisotropic Stress Models Improve Completion Design in the Baxter Shale. SPE Annual Technical Conference and Exhibition, SPE-115736-MS.

Hossain, M.M., Rahman, M.K., and Rahman, S.S. 2000. Hydraulic Fracture Initiation and Propagation: Roles of Wellbore Trajectory, Perforation and Stress Regime. *J. Pet. Sci. & Eng*. **27**: 129-149. https://doi.org/10.1016/s0920-4105(00)00056-5.

Hubbert, M.K. and Willis, D. 1957. Mechanics of Hydraulic Fracturing. *Trans. Am. Inst. Min. Eng*. **210**: 153–158.

Lecampion, B. 2012. Hydraulic Fracture Initiation from an Open-Hole: Wellbore Size, Pressurization Rate and Fluid-Solid Coupling Effects. Presented at the 46th US Rock Mechanics/Geomechanics Symposium, Chicago, Illinois, USA, 24-27 June. ARMA 12-601.

Lecampion, B., Desroches, J., Jeffrey, R.G., et al. 2015. Initiation versus Breakdown Pressure of Transverse Radial Hydraulic Fracture: Theory and Experiments. Presented at the 13th International Congress of Rock Mechanics, Montreal, Quebec, Canada, 10--13 May.

Li, Y., 1991. On Initiation and Propagation of Fractures from Deviated Wellbores. Ph.D. Thesis, The University of Texas at Austin.

Miller, C., Waters, G., and Rylander, E. 2011. Evaluation of Production Log Data from Horizontal Wells Drill in Organic Shales. Presented at the SPE North American Unconventional Gas Conference & Exhibition, The Woodlands, Texas, USA, 12–16 June. SPE-144326-MS. https://doi.org/10.2118/144326-MS.

Molenaar, M.M. and Cox, B.E. 2013. Field Cases of Hydraulic Fracture Stimulation Diagnostics Using Fiber Optic Distributed Acoustic Sensing (DAS) Measurements and Analyses. Presented at SPE Middle East Unconventional Gas Conference and Exhibition, Muscat, Oman, 28-30 January. SPE-164030-MS. https://doi.org/10.2118/164030-MS.

Schoenberg, M., Muir, F., and Sayers, C. 1996. Introducing ANNIE: A simple three parameter anisotropic velocity model for shales. *Journal of Seismic Exploration*, **5**, 35-49.

Slocombe, R., Acock, A., Chadwick, C., Wigger, E., Viswanathan, A., Fisher, K. and Reischman, R. 2013. Eagle Ford Completion Optimization Strategies Using Horizontal Logging Data. Presented at the Unconventional Resources Technology Conference, Denver, Colorado, USA, 12–14 August. URTEC-1571745-MS.

Somanchi, K., O'Brien, C., Huckabee, P., and Ugueto, G. 2016. Insights and Observations into Limited Entry Perforation Dynamics from Fiber-Optic Diagnostics. Presented at Unconventional Resources Technology Conference, San Antonio, Texas, USA, 1–3 August. https://doi.org/10.15530-URTEC-2016-2458389.

Suarez, R. and Bratton, T. R. 2009. Estimating horizontal stress from three-dimensional anisotropy. US Patent 8175807 B2.

Thiercelin, M.C. and Roegiers, J.C. 2000. Chapter 3 Formation Characterization: Rock Mechanics. *Reservoir Stimulation*, 3rd ed., Economides, M.J. and Nolte, K.G., John Wiley & Sons.

Ugueto, G.A., Huckabee, P.T., Molenaar, M.M., Wyker, B., and Somanchi, K. 2016. Perforation Cluster Efficiency of Cemented Plug and Perf Limited Entry Completions; Insights from Fiber Optic Diagnostics. Presented at SPE Hydraulic Fracturing Technology Conference, The Woodlands, Texas, USA, 9–11 February. SPE-179124-MS. https://doi.org/10.2118/179124-MS.

van de Ketterij, R.G. and de Pater, C.J. 1997. Experimental Study on the Impact of Perforations on Hydraulic Fracture Tortuosity. Presented at the SPE European Formation Damage Conference, The Hague, The Netherlands, 1–2 June. SPE-38149-MS. https://doi.org/10.2118/38149-MS.

Walker, K., Wutherich, K., Terry, J., Shreves, J. and Caplan, J. 2012. Improving Production in the Marcellus Shale Using an Engineered Completion Design: A Case Study. Presented at the SPE Annual Technical Conference and Exhibition, San Antonio, Texas, USA, 8–10 October. SPE-159666-MS. https://doi.org/10.2118/159666-MS.

Waters, G. and Weng, X. 2016. The Impact of Geomechanics and Perforations on Hydraulic Fracture Initiation and Complexity in Horizontal Well Completions. Presented at the SPE Annual Technical Conference and Exhibition, Dubai, UAE, 26-28 September. SPE-181684-MS. https://doi.org/10.2118/181684-MS.

Weijers, L. and de Pater, C.J. 1992. Fracture Reorientation in Model Tests. Paper SPE 23790, presented at SPE International Symposium on Formation Damage Control, Lafayette, Louisiana, 26–27 February. SPE-23790-MS. https://doi.org/10.2118/23790-MS.

Weijers, L. and de Pater, C.J. 1994. Interaction and Link-up of Hydraulic Starter Fractures Close to a Perforated Wellbore. Presented at SPE/ISRM Rock Mechanics in Petroleum Engineering Conference, Delft, The Netherlands, 29–31 August. SPE-28077-MS. https://doi.org/10.2118/28077-MS.

Weijers, L., de Pater, C.J., Owens, K.A., and Kogsboll, H.H. 1994. Geometry of Hydraulic Fractures Induced from Horizontal Wellbores. *SPE Prod & Fac* **9** (2): 87–92. SPE-25049-PA. https://doi.org/10.2118/25049-PA.

Wilson, T., Carr, T., Carney, B. J., Hewitt, J., Costello, I., Jordon, E., MacPhail, K., Uschner, N., Thomas, M., Akin, J., Magbagbeola, O., Morales, A., Johansen, A., Hogarth, L., and Naseem, K. 2016. Microseismic and model stimulation of natural fracture networks in the Marcellus Shale, West Virginia. SEG Technical Program Expanded Abstracts 2016b: 3088-3092.

Wutherich, K., Walker, K., Aso, I., Ajayi, B. and Cannon, T. 2012. Evaluating an Engineered Completion Design in the Marcellus Shale Using Microseismic Monitoring. Presented at the SPE Annual Technical Conference and Exhibition, San Antonio, Texas, USA, 8–10 October. SPE-159681-MS. https://doi.org/10.2118/159681-MS.

Yew, C.H. and Li., Y. 1988. Fracturing of a Deviated Well, *SPE Prod Eng* **3** (4): 429–437. SPE-16930-PA. https://doi.org/10.2118/16930-PA.

Yew, C.H., Schmidt, J.H., and Li, Y. 1989. On Fracture Design of Deviated Wells. Presented at the SPE Annual Technical Conference and Exhibition, San Antonio, Texas, USA, 8–11 October. SPE-19722-MS. https://doi.org/10.2118/19722-MS.

Yuan, Y.G., Abousleiman, Y., Weng, X., and Roegiers, J.C., 1995. Three-Dimensional Elastic Analysis on Fracture Initiation from a Perforated Borehole. SPE 29601.